

Magnetic Monopoles in Spin Ice

AUTHOR: Felix Flicker, Perimeter Scholars International

SUPERVISOR: Professor Michel Gingras, University of Waterloo

Abstract

The spin ice systems $Ho_2Ti_2O_7$ and $Dy_2Ti_2O_7$ are believed to demonstrate an emergent $U(1)$ gauge structure resembling a gas of magnetic monopoles connected by Dirac strings. I review the evidence for the existence of such a ‘Coulomb phase’ and apply different models in search of an incontrovertible demonstration of the effect. In related work I use the models developed for spin ices in order to characterize a ring of scattering which has been observed recently in neutron scattering experiments on the spin glass $Y_2Mo_2O_7$. I demonstrate that the nearest neighbour model is insufficient to explain this phenomenon, and propose extensions which could bring the theory in line with experiment.

Contents

1	Introduction	2
1.1	Magnetic Monopoles	2
1.2	Geometric Frustration	3
1.3	The Pyrochlore Lattice	5
1.4	Outline of Report	6
2	Methods	7
2.1	Coarse-grained Polarization Field	7
2.2	Large N Model	9
2.3	Ewald Summation of the Dipolar Hamiltonian	12
2.4	Mean Field Theory	14
3	Results and Discussion	17
3.1	The Ising Systems $Dy_2Ti_2O_7$ and $Ho_2Ti_2O_7$	17
3.1.1	The Nearest-Neighbour Model	17
3.1.2	Including Dipolar Effects	18
3.1.3	Pinch-Point Temperature Dependence	20

3.1.4	Spin Flip and Non-Spin Flip Scattering	22
3.2	The Heisenberg System $Y_2Mo_2O_7$	23
3.2.1	Next-Nearest Neighbour Terms	24
3.2.2	Analytic Solution	25
4	Conclusions and Further Work	27
5	Acknowledgments	29
A	Lattice Definitions	30
B	Interaction Matrices	30

1 Introduction

1.1 Magnetic Monopoles

The quantum theory of magnetic monopoles was first elucidated in 1931 by Paul Dirac[1], who demonstrated that the presence of even a single such entity in the universe would lead to the quantization of all electric charge. Gauge invariance in the presence of magnetic monopoles is assured by having every monopole connected to a partner of opposite magnetic charge by a gauge dependent (and hence unobservable) string of magnetic flux along a nodal line in the monopole wavefunction. This nodal line is now known as a ‘Dirac string’. Experimental tests for the existence of magnetic monopoles in free space have so far given negative or ambiguous results[2].

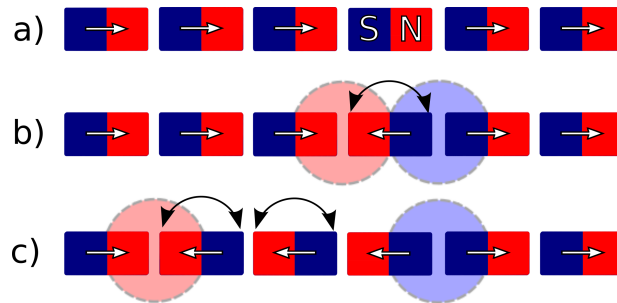


Figure 1: A demonstration of emergent monopoles in a lattice: (a) a chain of aligned bar magnets. (b) Flipping a magnet in the chain leads to a separated source and sink in the magnetization \mathbf{M} and magnetic field \mathbf{H} . (c) Flipping further magnets separates the source and sink, leading to an effective ‘isolated’ north pole to the left and south pole to the right. The chain of flipped magnets between these emergent monopoles is the classical analogue of the Dirac string. In dimensions other than 1 there is no unique choice of Dirac string (see Figure 2). This figure follows reference [3].

In a crystal lattice the story is different. As an illustration, consider a 1-D chain of

bar magnets end-to-end. If the magnets are allowed to orient themselves the sequence of poles will be alternating north to south, as is shown in Figure 1 (a). The magnetic field intensity \mathbf{B} , magnetization \mathbf{M} , and magnetic field \mathbf{H} , all form divergence free fields along the length of the chain. If we flip a magnet in the middle of the chain, at some finite energy cost, the situation changes. Although the condition $\nabla \cdot \mathbf{B} = 0$ is still fulfilled, we now have a divergence in \mathbf{M} and \mathbf{H} , such that $\nabla \cdot \mathbf{M} = -\nabla \cdot \mathbf{H} \neq 0$. We have a separated source and sink of both \mathbf{M} and \mathbf{H} . If we flip a neighbouring magnet, the divergence shifts along the chain. With analogy to Dirac’s proposed particles, we call the source of \mathbf{H} (sink of \mathbf{M}) a ‘magnetic monopole’, and the sink of \mathbf{H} (source of \mathbf{M}) an ‘anti-monopole’. This situation is shown in Figures 1 (b), (c).

This situation is observed in some rare earth titanates (Section 1.3), where spins replace the bar magnets of the above analogy. If the spins have only nearest neighbour interactions, the resulting monopoles are freely diffusing, requiring no energy to move once they are created. In general it will be necessary to take into account the long-ranged dipolar interactions between spins, in which case the emergent particles gain a Coulomb’s law interaction energy of the form

$$U(\mathbf{x}) = \frac{g_1 g_2}{|\mathbf{x}|} \quad (1)$$

with g_i the magnetic charge of each particle [4]. This situation is termed the ‘Coulomb phase’ [5, 6]. The magnetic monopoles are charged under a $U(1)$ gauge symmetry, just as electrons in the standard model [7]. For this reason authors sometimes refer to the Coulomb phase as having an ‘emergent $U(1)$ gauge symmetry’ [6, 8, 9].

Separating the emergent particles leaves a chain of flipped spins between the isolated poles. This is a classical analogue to the Dirac string. At finite temperatures, in dimensions greater than one, it becomes ambiguous as to what path the string follows, providing an analogue to the unobservability of the quantum case. For a given distribution of monopoles, the string can fluctuate at zero energy cost [10]. As the system’s temperature lowers we regain some measure of the string’s location, and when the surrounding lattice is completely ordered it is possible to identify the path of flipped magnets. These situations are shown in Figure 2.

1.2 Geometric Frustration

The third law of thermodynamics states that the entropy of an infinite perfect crystal, with a nondegenerate ground state, tends to zero as the temperature tends to absolute zero. An example of this is an Ising ferromagnet on an infinitely large simple cubic lattice. As we reduce the temperature of the crystal to zero, the spins drop into their minimum energy configuration, lining up in a spontaneously chosen direction. The

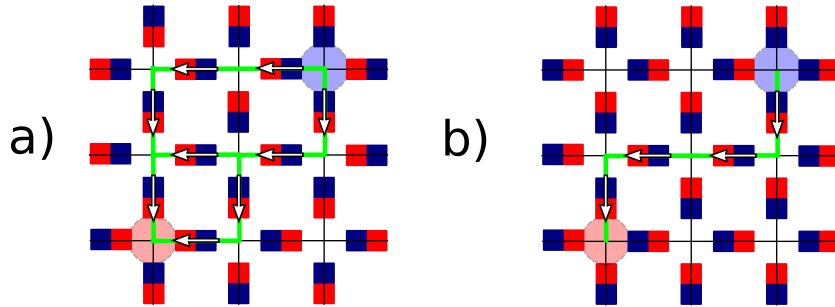


Figure 2: A 2D lattice of magnets. The ground state would have two north poles and two south poles at each vertex. In both cases here we are in an excited state, with violations of the 2-in 2-out rule (emergent monopoles). (a) With a disordered lattice, *i.e.* finite temperature, it is ambiguous as to where the line of reversed magnets lies. (b) In an otherwise ordered lattice the line of reversed magnets becomes well defined.

macroscopic observables, such as the energy or magnetization (the *macrostate*) are consistent with only one configuration of spins in the crystal (the *microstate*). Boltzmann’s expression for the entropy of a macrostate is, in natural units,

$$S = \ln(\Omega), \tag{2}$$

where Ω is the number of microstates consistent with that macrostate. In this case $\Omega = 1$ and so $S = 0$ ¹.

In geometrically frustrated systems it is not possible to satisfy the minimum energy constraint of every spin simultaneously. Minimizing one spin’s energy would force its neighbours to be in a higher energy state due to the geometry of the crystal. As a result, a compromise has to be made.

One of the earliest known examples of geometric frustration comes from a very well known crystal, solid H_2O . The common I_h phase of ice forms a structure in which the oxygen atoms occupy a diamond lattice and the hydrogen atoms sit along the nearest neighbour bond directions [6]. This leaves each oxygen with 4 neighbouring oxygens defining a tetrahedron, and a hydrogen along each of these bonds. The situation is shown in Figure 3. Which oxygen each hydrogen sits closest to was not clear until Pauling [11], in 1935, demonstrated that the choice is made arbitrarily across the crystal, with the constraint that each oxygen has two close-in hydrogens and two further away hydrogens. This constraint is one of two ‘Bernal-Fowler ice rules’, with the other rule being that all hydrogens are restricted to oxygen nearest neighbour bonds [12].

The arbitrary choice of hydrogen positioning, bearing in mind the ice rules, leads to

¹There are some subtleties here. In a finite system the boundary term leads to a nonzero overlap of the ‘all up’ spin configuration’s wavefunction with the ‘all down’ wavefunction. These states are degenerate in energy, so the ground state entropy of the finite system is actually $S = \ln(2)$. For a truly infinite system the boundary term vanishes, and the wavefunction overlap and entropy reduce to zero.

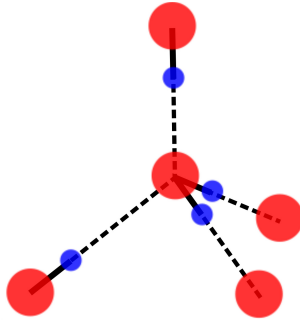


Figure 3: A section of the ice I_h structure, with oxygen atoms in red and hydrogen atoms in blue. Solid lines indicate covalent bonds (with an H_2O molecule in the centre of the tetrahedron), and dashed lines indicate hydrogen bonds. This tetrahedron can be seen to be obeying the Bernal-Fowler ice rule (2-in 2-out) at the central vertex; see Section 1.2.

a heavily disordered lattice even in the ground state. Unlike the case of the ferromagnet on a simple cubic lattice, the same macrostate can now be described by a huge number of microstates. This leads to a ‘ground state entropy’. Based on ice’s crystal structure, Pauling calculated the entropy *per hydrogen atom* to be

$$S_{ice}(T = 0) = \frac{1}{2} \ln \left(\frac{3}{2} \right). \quad (3)$$

The entropy in the ground state scales with the size of the crystal, and is thus macroscopic. Note that a nonzero ground state entropy does not constitute a violation of the third law of thermodynamics when that law is stated fully as at the start of this section. The ground state entropy of ice is now well established [13, 14].

1.3 The Pyrochlore Lattice

The compounds dysprosium titanate, $Dy_2Ti_2O_7$, holmium titanate, $Ho_2Ti_2O_7$, and yttrium molybdenate, $Y_2Mo_2O_7$, have a non-Bravais lattice structure. The magnetic ions (Dy^{3+} , Ho^{3+} , and Mo^{4+} respectively) occupy the sites of a pyrochlore lattice, space group $Fd\bar{3}m$, which can be thought of as a diamond lattice with a tetrahedron of lattice sites centred on (and in place of) each diamond site [15]. The pyrochlore sites sit exactly half way along each diamond bond. Equivalently, the pyrochlore lattice can be thought of as a face centred cubic lattice with a tetrahedron of sites at each FCC location. The conventional unit cell is pictured in Figure 4 (a). For lattice definitions used in this report, see Appendix A.

Hund’s rules for magnetic ions [16] work well in the case of the compounds of interest here. The spin configurations of the titanates are found to be ${}^6H_{15/2}$ for Dy^{3+} and 5I_8 for Ho^{3+} , from which we would expect a degeneracy of 16 or 17, respectively. This

degeneracy is lifted by a crystal field splitting [16] of order $2 - 300$ K [17], which is huge compared to the spin interaction energies which are of order 1 K (see Section 2.3). This splitting leads to an insurmountable barrier between the ground state doublet and the first excited state. What this means for our system is that the Dy^{3+} and Ho^{3+} magnetic moments are almost perfect Ising spins at low temperatures ($\lesssim 15$ K). The spins are aligned or anti-aligned along the nearest neighbour bonds of the diamond lattice. These Ising spins have a ferromagnetic (FM) nearest neighbour coupling [18]. Neighbouring bonds on the diamond lattice have a negative inner product $\mathbf{z}^\alpha \cdot \mathbf{z}^\beta = -\frac{1}{3}$ ($\alpha \neq \beta$), which means the FM coupling attempts to *anti-align* neighbouring spins. This constraint cannot be satisfied by all members of a tetrahedron, and the result is geometric frustration in exact analogy with ice. Consequently we term these crystals ‘spin ice’. The equivalent of the Bernal-Fowler ice rules lead to a ground state in which each tetrahedron has two spins pointing in and two pointing out, giving a sixfold degeneracy *per tetrahedron*. This situation is pictured in Figure 4 (b). Violations of the ice rules take the form of 3-in 1-out or 1-in 3-out tetrahedra. As in Section 1.1 we refer to these defects as magnetic monopoles.

The case of $Y_2Mo_2O_7$ is different to that of the titanates considered above. Hund’s rules give a spin configuration of 3F_2 for Mo^{4+} , and in this case the crystal field is zero to a first approximation [19]. This means that the spins are no longer constrained to the ground state doublet, and are not Ising-like. In fact, they are now well described by Heisenberg spins, with full rotational freedom in all three directions. Not being constrained to the ice rules, $Y_2Mo_2O_7$ is not a spin ice system. Instead, at low temperatures, it has been observed that the material’s dynamics become non-ergodic, meaning that the system is unable to explore the full space of possible configurations. This ‘freezing’ of the material is similar to the behaviour of glass at room temperature. In analogy, we refer to $Y_2Mo_2O_7$ as a ‘spin glass’ [15, 20].

1.4 Outline of Report

In Section 2 I will consider some theoretical models for spin ice and spin glass systems. I will demonstrate the equivalence of these models in different regimes. In Section 3 I detail the original work of this report, which comprises two main studies: in Section 3.1 I look for evidence of the Coulomb phase of spin ices; in Section 3.2 I apply the same techniques to a spin glass system, in an attempt to reproduce some strange experimental results. In Section 4 I will summarize my work and give suggestions for possible future enquiries.

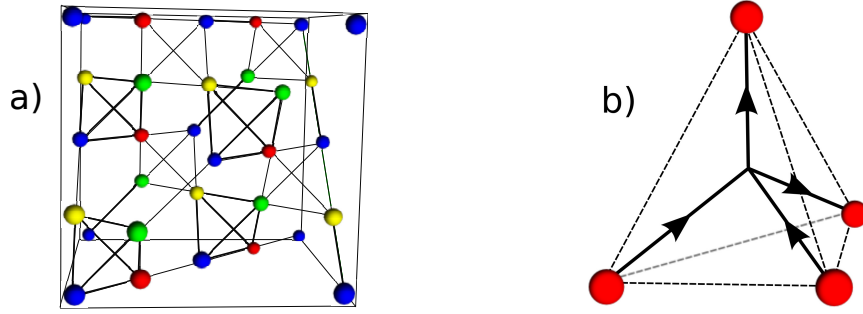


Figure 4: (a) The conventional unit cell for the pyrochlore lattice. The blue ions occupy a face centred cubic lattice; each combines with three other ions to form a tetrahedral motif. Right-way-up tetrahedron bonds are marked in bold, with upside-down tetrahedron bonds thin lines. Colours label sublattice sites for convenience, but all the ions pictured are identical. (b) A single tetrahedron of the pyrochlore lattice (dashed) with Ising spins along the local $\langle 111 \rangle$ directions. The solid lines indicate the diamond lattice. The Bernal-Fowler ice rules (2-in 2-out) can be seen to be obeyed.

2 Methods

2.1 Coarse-grained Polarization Field

The simplest model for spin ices, and the first to be studied historically, is the nearest neighbour model. The Hamiltonian is

$$\mathcal{H} = -J_1 \sum_{\langle ij \rangle} \mathbf{s}_i \cdot \mathbf{s}_j \quad (4)$$

with J_1 the nearest neighbour coupling, and \mathbf{s}_i the spin at site i . The sum is over all nearest neighbour pairs, and I will adopt the convention that ferromagnetic interactions are positive (hence the negative sign). This section follows the work of C. L. Henley [18], and related earlier work on ferroelectrics [21], in obtaining correlation functions in the low temperature limit.

First we define the polarization of a tetrahedron located at FCC site \mathbf{R}^α to be

$$\mathbf{P}(\mathbf{R}^\alpha) = t_\beta(\mathbf{R}^\alpha) \mathbf{z}^\beta \quad (5)$$

where $t_\beta(\mathbf{R}^\alpha)$ is the Ising spin (± 1) along the \mathbf{z}^β direction of the tetrahedron located at \mathbf{R}^α , and Einstein summation notation is assumed. Lattice conventions used in this report are given in Appendix A. I adopt the convention that Greek indices run from one to four, and Latin indices run from one to three (occasionally Latin indices may run over the entire lattice, in which case this should be apparent). The next step is to coarse grain the polarization so that it can be considered a smoothly varying function across the crystal. The ice rules now take the form

$$\nabla \cdot \mathbf{P}(\mathbf{x}) = 0 \quad (6)$$

with $\mathbf{x} = (x, y, z)$ the position in the crystal. The Helmholtz free energy, in the saddle-point approximation, now takes the following form [18]:

$$\mathcal{F}[\mathbf{P}] = \frac{T\kappa}{2V_{cell}} \int d^3\mathbf{x} |\mathbf{P}(\mathbf{x})|^2 \quad (7)$$

where $T = 1/\beta$ is the temperature, V_{cell} is the volume of the primitive unit cell, and κ is a dimensionless parameter which measures the stiffness of the lattice. From Equations 6 and 7 it follows that, in the limit $T \rightarrow 0$, Gaussian averages are weighted by the probability distribution

$$\text{Prob}[\mathbf{P}(\mathbf{x})] \propto \exp(-\beta\mathcal{F}[\mathbf{P}]) \prod_{\mathbf{x}} \delta^3(\nabla \cdot \mathbf{P}(\mathbf{x})). \quad (8)$$

Ice rules are rigidly enforced by the product of delta functions, so this distribution is strictly only valid in the ground state manifold.

Obtaining the real space correlation function $\langle \mathbf{P}_i(\mathbf{0}) \mathbf{P}_j(\mathbf{x}) \rangle$ is now relatively simple. Fourier transforming Equation 7 gives

$$\tilde{\mathcal{F}}[\mathbf{P}] = \frac{\kappa}{2} \sum_{\mathbf{k}} |\mathbf{P}(\mathbf{k})|^2. \quad (9)$$

I will use the convention in this report of writing reciprocal space vectors in units of 2π when given explicitly, with $\mathbf{k} = 2\pi(hkl)$. I will also adopt standard crystallographic notation. Applying the equipartition theorem would suggest that we now have $\langle \mathbf{P}_i(-\mathbf{k}) \mathbf{P}_j(\mathbf{k}) \rangle = \delta_{ij}/\kappa$. However, Equation 6 requires that the longitudinal component of the field be projected out, since in Fourier space we now have the constraint

$$\mathbf{k} \cdot \mathbf{P}(\mathbf{k}) = 0. \quad (10)$$

Projecting out the longitudinal component gives the result

$$\langle \mathbf{P}_i(-\mathbf{k}) \mathbf{P}_j(\mathbf{k}) \rangle = \frac{1}{\kappa} \left(\delta_{ij} - \frac{k_i k_j}{|\mathbf{k}|^2} \right) \quad (11)$$

and Fourier transforming back to real space gives the two-point correlation function:

$$\langle \mathbf{P}_i(\mathbf{0}) \mathbf{P}_j(\mathbf{x}) \rangle = \frac{4\pi}{\kappa} \left(\delta^3(\mathbf{x}) + \frac{1}{\mathbf{x}^3} \left(\delta_{ij} - \frac{3x_i x_j}{|\mathbf{x}|^2} \right) \right). \quad (12)$$

The result is remarkable. Spin ices demonstrate algebraic correlations ($1/|\mathbf{x}|^3$) without being in a critical state. This leads to long range order across the crystal. It was

believed for a long time that the ice rules were the cause of these correlations, but this is not the full story. In fact, algebraic correlations also arise from dipolar interactions between spins. I consider these interactions in Section 2.3. That the nearest neighbour model is reproducing a result from the full dipolar model is another remarkable feature of the theory. The link comes from the fact that the projector enforcing the ice rules (the term in parentheses in Equation 11) takes the same form as a dipolar interaction term. As a consequence, the ground states of the nearest neighbour and dipolar models are identical - a situation known as ‘projective equivalence’ [22].

2.2 Large N Model

The Ising spins of spin ices have a discrete symmetry group \mathbb{Z}_2 , which is isomorphic to the group $O(1)$. The Heisenberg spins of spin glasses have continuous symmetry group $O(3)$. The idea of a large N expansion is to consider higher dimensional spins with symmetry group $O(N)$. In the limit $N \rightarrow \infty$, the corresponding Hamiltonian is exactly solvable [23]. In general, an expansion in $1/N$ is then made about $1/N = 0$. In the systems of interest here, the zeroth order result is sufficient. This section follows C. L. Henley [18], and the generalization to higher temperature made by P. H. Conlon and J. T. Chalker [24, 25] and S. Isakov [26].

First, some comments on the validity of the large N approach. Although the results are strictly only valid for spins with an infinite number of components, they are found to be in good agreement with Monte Carlo simulations of the Heisenberg system $N = 3$ [24]. As noted by Isakov and others, large N becomes non-analytic at $N = 2$. The problem is the breakdown of the orthogonal group $O(N)$ from continuous to discrete as N lowers to 1. As an added subtlety the $N = 2$ case collapses to an $N = 1$ state due to thermal fluctuations, in a process known as *order by disorder* [26]. For this reason, large N would be expected to fail for Ising spins, $N = 1$. In fact it works well, as evidenced by Monte Carlo simulations [26]. This fact remains to be explained.

Proceeding from Section 2.1, we begin by allowing the spins t_α to take any real value (no longer ± 1). I will switch to Dirac notation by defining the inner product $\langle t|t \rangle = \sum_{\alpha=1}^4 t_\alpha^2$. In this case, the probability distribution of spins can now be written as follows:

$$\text{Prob} [|t\rangle] \propto \exp(-\lambda \langle t|t \rangle / 2) \exp(-\beta \mathcal{H} [|t\rangle]). \quad (13)$$

The ice rules are no longer rigidly enforced, but excitations are restricted by the factor $\exp(-\beta \mathcal{H})$. The Lagrange multiplier $\lambda = 2$ ensures that in the ground state manifold $\langle t|t \rangle = 1$, *i.e.* the *average* spin length is still 1 at each site.

The aim of this section is to find the correlation function $\langle \tilde{t}_\alpha(\mathbf{k}) | \tilde{t}_\beta(\mathbf{k}) \rangle$ between Fourier

transformed spins. This function leads to the structure factor of the crystal, and hence the neutron scattering intensity which can be compared with experiment.

Defining the 4×2 matrices

$$E(\mathbf{k})_{m\alpha} = \exp\left((-1)^m \frac{i}{2} \mathbf{k} \cdot \mathbf{z}_\alpha\right) \quad (14)$$

we can write the Fourier transformed Hamiltonian as

$$\tilde{\mathcal{H}} = -\frac{1}{2} J_1 \langle \tilde{t} | EE^\dagger | \tilde{t} \rangle \quad (15)$$

where EE^\dagger is now a 4×4 matrix. Substituting into the Fourier transform of Equation 13 leads to

$$\text{Prob} [|\tilde{t}\rangle] \propto \exp\left(-\frac{1}{2} \langle \tilde{t} | \Omega | \tilde{t} \rangle\right) \quad (16)$$

with

$$\Omega = \lambda \mathbb{1}_4 - \beta EE^\dagger. \quad (17)$$

Finally, by carrying out the standard Gaussian functional integral, we obtain the Fourier transformed two-point correlation function

$$\langle \tilde{t}_\alpha(-\mathbf{k}) | \tilde{t}_\beta(\mathbf{k}) \rangle = [\Omega^{-1}]_{\alpha\beta}. \quad (18)$$

Adding in next nearest neighbour terms is also possible. From a different line of reasoning, Conlon and Chalker arrive at Equation 18 with EE^\dagger replaced by the ‘interaction matrix’ $\sum_n J_n V^{(n)}(\mathbf{k})$. The interaction matrices $V^{(n)}(\mathbf{k})$ are found by Fourier transforming the n^{th} nearest neighbour structure and adding multiples of the identity. The process and resulting matrices are given in Appendix B. In order to move away from the ground state manifold, a self-consistency equation is required to maintain the normalization $\langle s|s \rangle = 1$. The equation is as follows [24, 25]:

$$1 = \frac{1}{4N} \sum_{\mathbf{k} \in BZ} \text{Tr} \left[\lambda \mathbb{1}_4 - \beta \sum_n J_n V^{(n)}(\mathbf{k}) \right]^{-1} \quad (19)$$

where the number of sites in the whole crystal is $4N$. The value of the Lagrange multiplier λ is determined numerically from this condition. In the case of Heisenberg spins, the left hand side is replaced by the length of each spin component, *i.e.* $1/3$. The value of λ is shown in Figure 5 for the case of Heisenberg spins, for a range of temperatures T/J_1 with $J_3/J_1 = \pm 0.01$, 0.0 and all other $J_{n>1} = 0$. This can be compared to Figure 2 of [24].

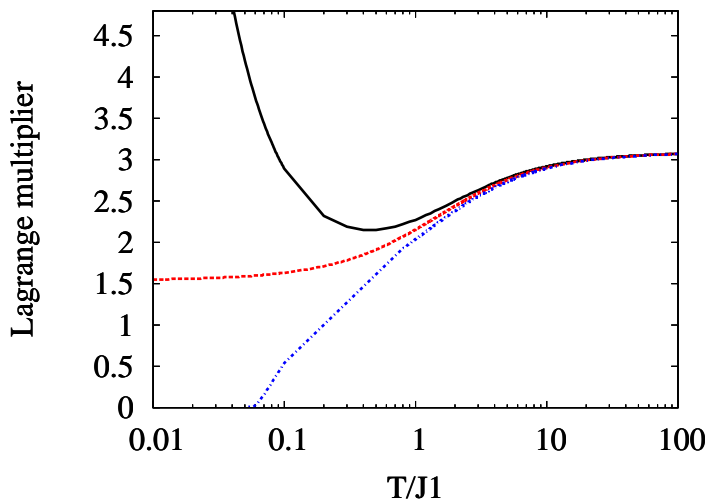


Figure 5: The value of the Lagrange multiplier λ against temperature T/J_1 for the cases $J_3/J_1 = 0.01$ (black, solid), $J_3/J_1 = 0.00$ (red, dashed), and $J_3/J_1 = -0.01$ (blue, dot-dashed). All other $J_{n>1} = 0$. The values were found numerically from Equation 19, and can be compared with the results in Figure 2 of [24].

The modulus square of the structure factor² is given by the sum of all the elements of $\langle \tilde{t}_\alpha(-\mathbf{k}) | \tilde{t}_\beta(\mathbf{k}) \rangle$,

$$|f(\mathbf{k})|^2 = \sum_{\alpha,\beta} [\Omega^{-1}(\mathbf{k})]_{\alpha\beta}. \quad (20)$$

In the case of Heisenberg spins the quantity $|f(\mathbf{k})|^2$ is equal to the neutron scattering intensity $S(\mathbf{k})$ (up to a constant scale factor) and we are done. In the case of Ising spins we have to project out the longitudinal spin components in order to get the neutron scattering intensity. By defining the projector

$$\mathcal{P}_{ij} = \delta_{ij} - \frac{k_i k_j}{|\mathbf{k}|^2} \quad (21)$$

and defining for convenience the 3×4 matrix $M^{i\alpha} = [\mathbf{z}^\alpha]^i$, we have the following formula for the neutron scattering intensity for spin ices:

$$S(\mathbf{k}) = \mathcal{P}^{ij}(\mathbf{k}) M_{i\alpha} [\Omega^{-1}(\mathbf{k})]^{\alpha\beta} M_{\beta j}^\dagger. \quad (22)$$

²The quantity given here is the squared modulus of the structure factor, $|f(\mathbf{k})|^2$. As the structure factor $f(\mathbf{k})$ itself is of little interest, I will continue a common practice in the literature and will use ‘structure factor’ to refer to $|f(\mathbf{k})|^2$ in this report.

2.3 Ewald Summation of the Dipolar Hamiltonian

To move beyond the nearest neighbour model of the previous sections, it is necessary to consider the long-range dipolar interactions between spins. Dipole fields drop off as $1/|\mathbf{x}|^3$ with distance $|\mathbf{x}|$, which means that sums over dipolar fields are conditionally convergent in three dimensional space. Indeed, they are saved from *divergence* only by their angular dependence. An ingenious way of converting this conditionally convergent sum into two rapidly convergent sums was devised by Peter Ewald in 1921 [27]. The method is applied to pyrochlores by P. Enjalran and M. J. P. Gingras [28, 29], A. G. Del Maestro [31], and L. D. C. Jaubert [32]. These references provide a step-by-step guide to the calculation; I will provide a sketch of the derivation here. For simplicity I will consider the case of Ising spins, but the generalization to Heisenberg spins is given in the references.

The Hamiltonian including the nearest neighbour term and the dipolar interaction between spins is as follows:

$$\begin{aligned} \mathcal{H} = & -J_1 \sum_{\langle ij \rangle} \left(\sum_{\alpha} t_i^{\alpha} \mathbf{z}^{\alpha} \right) \cdot \left(\sum_{\beta} t_j^{\beta} \mathbf{z}^{\beta} \right) \\ & + D \sum_{i>j} \sum_{\alpha>\beta} \left[\frac{\left(t_i^{\alpha} \mathbf{z}^{\alpha} \right) \cdot \left(t_j^{\beta} \mathbf{z}^{\beta} \right)}{|\mathbf{R}_{\alpha\beta}^{ij}|^3} - \frac{3 \left(t_i^{\alpha} \mathbf{z}^{\alpha} \right) \cdot \left(\mathbf{R}_{\alpha\beta}^{ij} \right) \left(t_j^{\beta} \mathbf{z}^{\beta} \right) \cdot \left(\mathbf{R}_{\alpha\beta}^{ij} \right)}{|\mathbf{R}_{\alpha\beta}^{ij}|^5} \right] \end{aligned} \quad (23)$$

where $\mathbf{R}_{\alpha\beta}^{ij} = \mathbf{R}^j - \mathbf{R}^i + \mathbf{r}^{\beta} - \mathbf{r}^{\alpha}$ [33, 34]. Spins have been written along the local $\langle 111 \rangle$ axes: $\mathbf{s}_i = \sum_{\alpha} t_i^{\alpha} \mathbf{z}^{\alpha}$, where $t_i^{\alpha} = \pm 1$ is the Ising spin on sublattice α at site i , and \mathbf{z}^{α} is the corresponding $\langle 111 \rangle$ direction. The sum over i covers all the FCC sites in the entire (infinite) lattice, and the sums over α and β cover sublattice sites. I have left sums explicit for clarity. The dipolar energy scale $D = \frac{\mu^2}{4\pi}$, where μ is the magnetic moment of the magnetic ion, which is $\simeq 10\mu_B$ in the spin ice systems considered here. For these systems, the nearest neighbour dipole energy scale, found by truncating the dipole fields at the nearest neighbour distance R_{nn} , is found to be $D_{nn} = \frac{5}{3} \frac{\mu^2}{4\pi R_{nn}^3} = +2.35 \text{ K}$ [30]. The factor of $\frac{5}{3}$ comes from the angle between local Ising axes. For comparison, J_1 is -0.52 K in holmium titanate and -1.24 K in dysprosium titanate [30]. The effective nearest neighbour coupling $J_{eff} = J_1 + D_{nn}$ is therefore positive (FM) for both materials, leading to geometric frustration.

We would like to Fourier transform the Hamiltonian as before. First, we write the Hamiltonian as

$$\mathcal{H} = -\frac{1}{2} \langle t_{\alpha} | \sum_{i,j} \mathcal{J}_{ij}^{\alpha\beta} | t_{\beta} \rangle \quad (24)$$

with

$$\mathcal{J}^{\alpha\beta}(\mathbf{R}_{\alpha\beta}^{ij}) = J_1 \mathbf{z}^\alpha \cdot \mathbf{z}^\beta \delta_{R_{ij}, R_{nn}} - D \left(\frac{\mathbf{z}^\alpha \cdot \mathbf{z}^\beta}{|\mathbf{R}_{\alpha\beta}^{ij}|^3} - \frac{3\mathbf{z}^\alpha \cdot (\mathbf{R}_{\alpha\beta}^{ij}) \mathbf{z}^\beta \cdot (\mathbf{R}_{\alpha\beta}^{ij})}{|\mathbf{R}_{\alpha\beta}^{ij}|^5} \right). \quad (25)$$

Note that this is the same method as in Section 2.2. Fourier transforming $\mathcal{J}(\mathbf{R}_{ij}^{\alpha\beta})$ would give the reciprocal space ‘interaction matrix’, taking the place of $\sum_n J_n V^{(n)}$ in that section.

The dipole term

$$\mathcal{J}^{\alpha\beta}(\mathbf{R}_{ij}^{\alpha\beta})_{dipolar} = \frac{\mathbf{z}^\alpha \cdot \mathbf{z}^\beta}{|\mathbf{R}_{\alpha\beta}^{ij}|^3} - \frac{3\mathbf{z}^\alpha \cdot (\mathbf{R}_{\alpha\beta}^{ij}) \mathbf{z}^\beta \cdot (\mathbf{R}_{\alpha\beta}^{ij})}{|\mathbf{R}_{\alpha\beta}^{ij}|^5}$$

can be rewritten as

$$\mathcal{J}^{\alpha\beta}(\mathbf{R}_{ij}^{\alpha\beta})_{dipolar} = -(\mathbf{z}^\alpha \cdot \nabla_{\mathbf{x}})(\mathbf{z}^\beta \cdot \nabla_{\mathbf{x}}) \left\{ \frac{1}{|\mathbf{R}_{\alpha\beta}^{ij} - \mathbf{x}|} \right\}_{\mathbf{x}=0} \quad (26)$$

and applying the Fourier transform gives the result

$$\mathcal{J}^{\alpha\beta}(\mathbf{k})_{dipolar} = -(\mathbf{z}^\alpha \cdot \nabla_{\mathbf{x}})(\mathbf{z}^\beta \cdot \nabla_{\mathbf{x}}) \left\{ \sum'_i \frac{\exp(-i\mathbf{k} \cdot \mathbf{R}_{\alpha\beta}^{ij})}{|\mathbf{R}_{\alpha\beta}^{ij} - \mathbf{x}|} \right\}_{\mathbf{x}=0} \quad (27)$$

where the sum \sum'_i is over all $\mathbf{R}_{\alpha\beta}^{ij}$ except those where $\mathbf{R}^j - \mathbf{R}^i = 0$. It is this sum which is conditionally convergent, and which the Ewald method treats.

The conditionally convergent sum suffers from summing long-ranged terms out to infinite distance in real space. A sum over reciprocal space would suffer from similar difficulties. In the Ewald method, the real space sum from zero to infinity is split into two parts: a real space sum from zero to some distance α , and a reciprocal space sum from (real space distances) α to infinity. Both of these sums are rapidly convergent, as the long tails are cut off. The final result is this:

$$\mathcal{J}^{\alpha\beta}(\mathbf{k})_{dipolar} = W^{\alpha\beta}(\mathbf{k}) + X^{\alpha\beta}(\mathbf{k}) - \frac{4\alpha^3}{3\sqrt{\pi}} \quad (28)$$

with

$$W^{\alpha\beta}(\mathbf{k}) = 4\pi \sum_{\mathbf{G}} \frac{\mathbf{z}^\alpha \cdot (\mathbf{k} - \mathbf{G}) \mathbf{z}^\beta \cdot (\mathbf{k} - \mathbf{G})}{|\mathbf{k} - \mathbf{G}|^2} \exp(-\mathbf{G} \cdot \mathbf{r}^{\alpha\beta}) \exp\left(\frac{-|\mathbf{k} - \mathbf{G}|^2}{4\alpha^2}\right) \quad (29)$$

$$X^{\alpha\beta}(\mathbf{k}) = \sum_i' [S1^{\alpha\beta}(\mathbf{R}_{\alpha\beta}^{ij}) - S2^{\alpha\beta}(\mathbf{R}_{\alpha\beta}^{ij})] \exp(-i\mathbf{k} \cdot \mathbf{R}_{\alpha\beta}^{ij}) \quad (30)$$

$$S1^{\alpha\beta}(\mathbf{R}_{\alpha\beta}^{ij}) = \mathbf{z}^\alpha \cdot \mathbf{z}^\beta \left\{ \frac{2\alpha}{\sqrt{\pi}|\mathbf{R}_{\alpha\beta}^{ij}|^2} \exp(-\alpha^2|\mathbf{R}_{\alpha\beta}^{ij}|^2) + \frac{\text{erfc}(\alpha|\mathbf{R}_{\alpha\beta}^{ij}|)}{|\mathbf{R}_{\alpha\beta}^{ij}|^3} \right\} \quad (31)$$

$$S2^{\alpha\beta}(\mathbf{R}_{\alpha\beta}^{ij}) = \mathbf{z}^\alpha \cdot \mathbf{R}_{\alpha\beta}^{ij} \mathbf{z}^\beta \cdot \mathbf{R}_{\alpha\beta}^{ij} \left\{ \frac{2\alpha}{\sqrt{\pi}|\mathbf{R}_{\alpha\beta}^{ij}|^2} \left(2\alpha^2 + \frac{3}{|\mathbf{R}_{\alpha\beta}^{ij}|^2} \right) \exp(-\alpha^2|\mathbf{R}_{\alpha\beta}^{ij}|^2) \right. \\ \left. + \frac{3\text{erfc}(\alpha|\mathbf{R}_{\alpha\beta}^{ij}|)}{|\mathbf{R}_{\alpha\beta}^{ij}|^5} \right\}. \quad (32)$$

The sum distance α enters the expressions as a convergence parameter. If the (now rapidly convergent) sums are taken to infinity the α dependence disappears. In practice, sums are taken out to around 10 sites in real and reciprocal space, and the result has a small dependence on α .

2.4 Mean Field Theory

Self-consistent mean field theory (MFT) is a very generic method for solving large and complex systems approximately. The general idea, with specific reference to lattice models, is this: rather than treat the interactions of each lattice degree of freedom with all the others in the system, we instead treat only a local region. The rest of the material's contribution is treated as a 'mean field'. Self-consistency conditions are then applied in order to maintain physically sensible quantities.

MFT has already entered this report in Section 2.2, which will serve as a good illustration. In that case, rather than treat the interactions of an infinite number of $S = 1$ Ising spins we assumed averages could be modeled by a Gaussian distribution - that is, a mean field in which cumulants other than the first and second are zero. This required the spins' lengths and their Ising nature to be disregarded. We maintained physicality with the Lagrange multiplier λ , which ensured the self-consistency condition $\langle \mathbf{s}_i^2 \rangle = 1$ at each site. The self-consistency equation in that case was Equation 19.

We are now interested in applying MFT to a lattice of long-ranged dipole terms. This is done explicitly in references [28, 29, 30]. Rather than rederive the work of those papers, I will instead provide a proof that the MFT found there is equivalent in the high temperature limit to the large N theory previously discussed.

The result for the neutron differential cross section from [28, 29] is:

$$\frac{d\sigma}{d\Omega} = C |f_M(\mathbf{K})|^2 \sum_{\alpha} \frac{|\mathbf{F}_{\perp}^{\alpha}(\mathbf{k})|^2}{1 - \beta\Lambda^{\alpha}(\mathbf{k})} \quad (33)$$

with C a constant, and $f_M(\mathbf{K})$ the magnetic form factor for the relevant ions. The scattering vector $\mathbf{K} = \mathbf{k} + \mathbf{G}$ is the position in reciprocal space (position in 1st Brillouin zone plus a translation between Brillouin zones). The scattering intensity $S(\mathbf{k})$, previously discussed, is given in this case by the above expression with the form factor removed. The 4 three component vectors $\mathbf{F}_{\perp}^{\alpha}$ are defined by

$$\mathbf{F}_{\perp}^{\alpha}(\mathbf{k}) = \sum_{\beta=1}^4 \mathbf{z}_{\perp}^{\beta} U^{\beta\alpha}(\mathbf{k}) \exp(i\mathbf{G} \cdot \mathbf{r}^{\beta}) \quad (34)$$

with

$$\mathbf{z}_{\perp}^{\beta} = \mathbf{z}^{\beta} - \frac{\mathbf{k} \cdot \mathbf{z}^{\beta}}{|\mathbf{k}|^2} \mathbf{k} \quad (35)$$

and the (Fourier transformed) Hamiltonian has been written in diagonal form

$$\tilde{\mathcal{H}}_{\beta\gamma} = [U\Lambda U^{\dagger}]_{\beta\gamma} = \sum_{\alpha} U_{\beta\alpha} \Lambda^{\alpha} U_{\alpha\gamma}^{\dagger} \quad (36)$$

with Λ^{α} the eigenvalue of eigenvector α , and Λ the 4×4 matrix of eigenvalues.

I will treat for simplicity the 1st Brillouin zone, setting the phase factors of Equation 34 to one. In this case we can employ Einstein summation notation, writing a 4×3 matrix $F^{a\alpha} = [F^{\alpha}]^a$ and recalling the definition $M^{a\alpha} = [\mathbf{z}^{\alpha}]^a$. Equation 34 can then be rewritten

$$F_{\perp}^{i\alpha} = \mathcal{P}^{ij} M_{j\beta} U^{\beta\alpha} \quad (37)$$

using the projector of Equation 21. Reference to \mathbf{k} dependence is neglected for clarity. Dropping the form factor, the MFT result of Equation 33 becomes

$$S_{MFT} = \sum_{\alpha=1}^4 \frac{(\mathcal{P}^{ij} M_{j\beta} U^{\beta\alpha})^{\dagger} (\mathcal{P}^{il} M_{l\gamma} U^{\gamma\alpha})}{1 - \beta\Lambda^{\alpha}}. \quad (38)$$

In the high temperature (low β) limit, this takes the approximate form

$$S_{MFT} \simeq \sum_{\alpha=1}^4 (\mathcal{P}^{ij} M_{j\beta} U^{\beta\alpha})^{\dagger} (\mathcal{P}^{il} M_{l\gamma} U^{\gamma\alpha}) (1 + \beta\Lambda^{\alpha}) \quad (39)$$

or, expanding the parentheses and using that $UU^{\dagger} = U^{\dagger}U = \mathbb{1}_4$ (as $\tilde{\mathcal{H}}$ is Hermitian),

$$S_{MFT} \simeq (M_{j\beta})^\dagger (\mathcal{P}^{ij})^\dagger \mathcal{P}^{il} M_{l\gamma} [\mathbb{1}_4 + \beta U \Lambda U^\dagger]_{\beta\gamma}. \quad (40)$$

Being a projector, \mathcal{P} obeys the relations $\mathcal{P}^\dagger = \mathcal{P}$ and $\mathcal{P}^2 = \mathcal{P}$. Using these relations, and re-ordering the terms (which is allowed as they are all scalar in the summation notation), gives the result

$$S_{MFT} \simeq \mathcal{P}^{ij} M_{i\alpha} [\mathbb{1}_4 + \beta U \Lambda U^\dagger]^{\alpha\beta} M_{\beta j}^\dagger. \quad (41)$$

The large N result, Equation 22, can be written in a similar form; we have there that

$$S_{large N} = \mathcal{P}^{ij} M_{i\alpha} \left[\left(\lambda \mathbb{1}_4 - \beta \sum_n J_n V^{(n)} \right)^{-1} \right]^{\alpha\beta} M_{\beta j}^\dagger \quad (42)$$

where the Lagrange multiplier λ should not be confused with the eigenvalues $\Lambda^\alpha(\mathbf{k})$. The interaction matrices entered by stating that $\tilde{\mathcal{H}} = -\frac{1}{2} \langle \tilde{t} | \sum_n J_n V^{(n)} | \tilde{t} \rangle$. Diagonalizing $\tilde{\mathcal{H}}$ and following Section 2.1 leads to the form

$$S_{large N} = \mathcal{P}^{ij} M_{i\alpha} \left[(\lambda \mathbb{1}_4 - \beta U \Lambda U^\dagger)^{-1} \right]^{\alpha\beta} M_{\beta j}^\dagger. \quad (43)$$

In the high temperature limit, expanding to first order in β , this gives

$$S_{large N} \simeq \lambda^{-1} \mathcal{P}^{ij} M_{i\alpha} \left[\mathbb{1}_4 + \frac{\beta}{\lambda} U \Lambda U^\dagger \right]^{\alpha\beta} M_{\beta j}^\dagger$$

and the λ^{-1} in the front can be absorbed into the omitted prefactor, giving the final result:

$$S_{large N} \simeq \mathcal{P}^{ij} M_{i\alpha} \left[\mathbb{1}_4 + \frac{\beta}{\lambda} U \Lambda U^\dagger \right]^{\alpha\beta} M_{\beta j}^\dagger. \quad (44)$$

In the high temperature limit, the large N MFT (Equation 44) and the MFT of [28] (Equation 41) are therefore equivalent, with an important caveat. Mean field theories necessarily have a critical temperature built into them, below which the model breaks down. In the case of Equation 33, this critical temperature occurs when the denominator becomes negative. This leads to $T_c = \max_{\mathbf{k} \in BZ} (\Lambda^\alpha(\mathbf{k}))$, *i.e.* the maximum value of the maximum eigenvalue across the whole Brillouin zone. The presence of the Lagrange multiplier in the large N result acts to push T_c to zero. This follows from another general feature of MFTs: the critical temperature $T_c \sim 1/N$, with N the number of degrees of freedom at each lattice site (in this case the dimension of the spin). As the large N expansion has $N \rightarrow \infty$, it has $T_c = 0$.

In this section I have shown that the MFT formula employed in [28, 29] is equivalent to the large N model of [18, 24, 25] in the high temperature limit. Although I considered Ising spins here, the generalization of each model to Heisenberg spins does not affect this result. The high temperature limit will be important in Section 3.2 when considering spin glass dynamics at temperatures of order 200 K.

3 Results and Discussion

3.1 The Ising Systems $Dy_2Ti_2O_7$ and $Ho_2Ti_2O_7$

The emergent $U(1)$ gauge structure of spin ice is believed to occur at temperatures high enough that a significant number of tetrahedra violate the ice rules, but low enough that double defects (4-in 0-out and 4-out 0-in) do not occur. In practice, this temperature range is around 2 – 6 K. We term this regime the Coulomb phase (Section 1.1). At higher temperatures the system enters a paramagnetic phase.

Experimental evidence for the existence of the Coulomb phase in spin ices exists, but we are still lacking an undisputed demonstration. Attempts to remedy this take many approaches. One is to consider the spin ice material to be a ‘magnetolyte’: a magnetically charge-neutral material which contains equal numbers of positive and negative magnetic charges [4, 35, 36, 37]. Applying magnetic fields should separate bound monopole pairs leading to observable effects [38, 39, 40]. Another approach focuses on neutron scattering data, which show sharp ‘pinch points’ across a range of temperatures. It is with this approach that I will be concerned in this report.

3.1.1 The Nearest-Neighbour Model

By the method of sections 2.1 and 2.2 I generated Mathematica and FORTRAN codes to calculate the structure factor and neutron scattering pattern of spin ice. The large N result allows the calculation to run at any temperature.

The structure factor of spin ice shows features referred to in the literature as ‘bow ties’ [18, 41], owing to their shapes. At the knots of the bow ties are ‘pinch points’. At zero temperature (Figure 6 (a)) the pinch points are singular: the value at those points depends upon the direction from which they are approached. The neutron scattering pattern, Figure 6 (b), features similar pinch point singularities. In the finite temperature case (Figures 6 (c) and (d)) the pinch points round off and become nonsingular.

The infinitely sharp points at $T = 0$ K are of great interest, as they suggest infinitely long-ranged interactions in the crystal. It was believed until very recently [42] that the pinch points in spin ices arose because of the ice rules, which lead to long range correlations. We now know this is not the whole truth. In fact, the pinch points

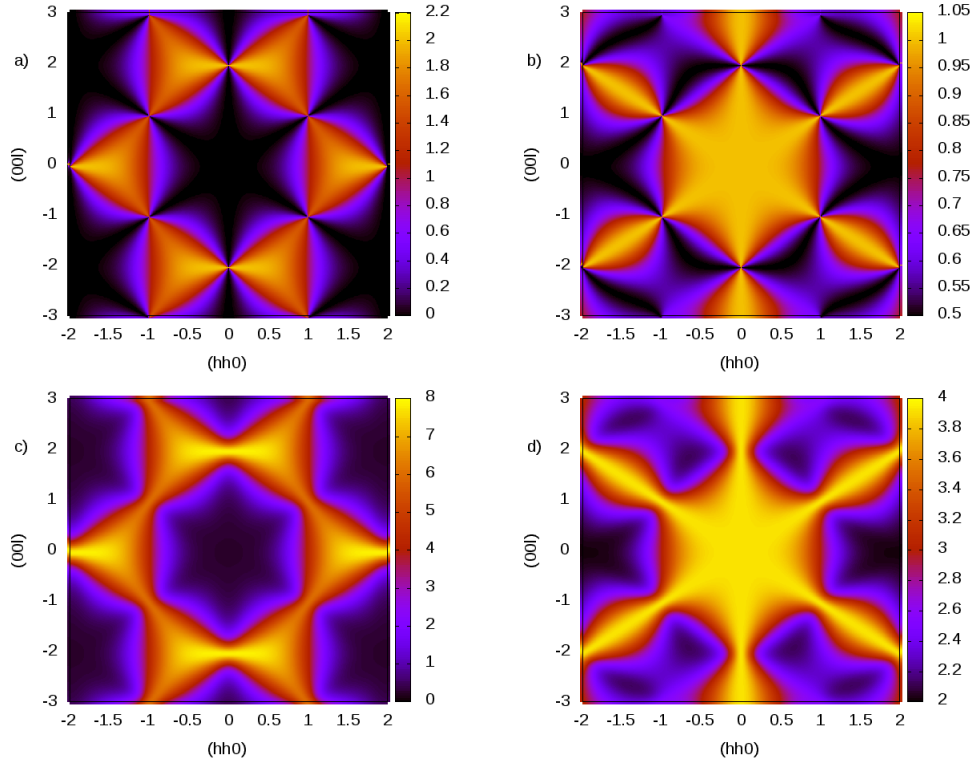


Figure 6: For the nearest neighbour model: (a),(b) the structure factor and neutron scattering factor of spin ice for the $T = 0$ case; (c),(d) the same plots for $T = 0.5 J_1$. All plots are in the (hhl) plane. In the zero temperature case ‘pinch point’ singularities occur at (002) and symmetry related locations. At finite temperatures the pinch points blur out and become nonsingular. In experiments the pinch points persist to high temperature, suggesting the dipolar interactions must be taken into account.

observed in experiment persist to high temperatures (upwards of 10 K). In this regime they must be due to dipolar interactions. Their presence in the nearest neighbour model at zero temperature is another demonstration of ‘projective equivalence’ (Section 2.1): the ground states of the two models are identical. In the high temperature regime the pinch points are not due to the ice rules, but this does not rule out the idea that there is a crossover at low temperature wherein the ice rules take over and give the leading contribution to pinch point scattering. Distinguishing the contributions to the pinch points from the ice rules and from the dipoles is thus of vital importance in demonstrating the existence of magnetic monopoles in spin ices.

3.1.2 Including Dipolar Effects

Using the Ewald technique of Section 2.3 I constructed a FORTRAN code to model dipolar spin ice, including nearest neighbour terms. I took real and reciprocal space sums to ten unit cells in every direction, and used the large N model to find the struc-

ture factors and neutron scattering patterns. The code was executed on the HYDRA supercomputing cluster in the University of Waterloo.

Previous studies in dipolar spin ice have used mean field theory [28, 29]. In this report I take a different approach, treating the dipolar term as a small perturbation to the large N nearest neighbour model. This requires some comment. First, the dipolar contribution to real spin ices is actually larger than the nearest neighbour contribution, as mentioned in Section 2.3. Second, the large N model takes the number of spin components N to infinity, before approximating finite values of N such as $N = 1$ for Ising spins. To properly include the dipolar term would require taking the dimension of the dipolar fields to infinity in a similar manner. Instead, I will use the 3-dimensional form previously given. Despite these issues the method makes a number of improvements on the nearest neighbour model, as I will show.

The dipolar structure factor and scattering pattern feature singular pinch points at all temperatures, in agreement with experiment. Plots are shown in Figure 7. The other notable difference between this model and the nearest neighbour model occurs in the high temperature limit. As $T \rightarrow \infty$ in the dipolar case, the scattering pattern resembles the low temperature nearest neighbour model. In the same limit the latter model develops broad lines along the $\{111\}$ directions, as can be seen in Figure 6 (d).

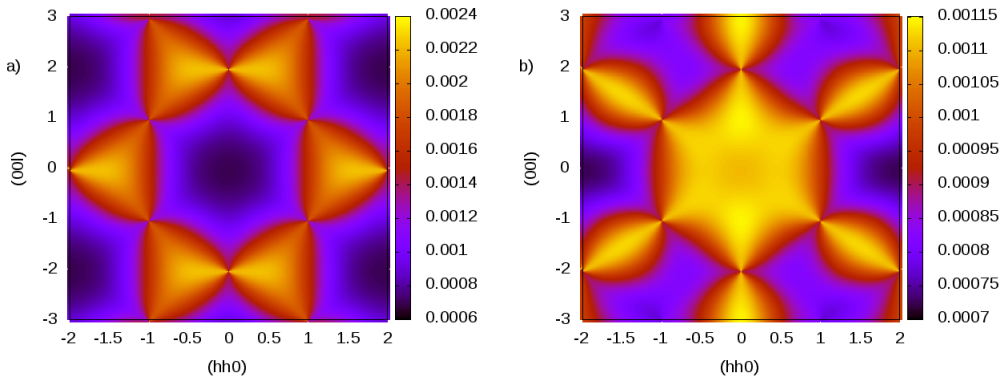


Figure 7: (a) The structure factor at $T = 0.5|J_1|$ for the dipolar spin ice Hamiltonian, with parameters set to those of dysprosium titanate (Equation 23, with $J_1 = -1.24$ K and $D = 2.35$ K). (b) The corresponding neutron scattering pattern. Note that the temperature is that of Figures 6 (c) and (d), but the pinch points in this dipolar case remain sharp.

These results demonstrate that the presence of pinch points at high temperatures in spin ices is due to the dipolar interactions between spins, and not due to the enforcement of the ice rules on the nearest neighbour model. As such, the presence of such features in observed scattering is not sufficient to demonstrate the existence of the Coulomb phase. It may still be the case, however, that properties of the pinch points such as their temperature dependence may be indicative of the presence of magnetic monopoles.

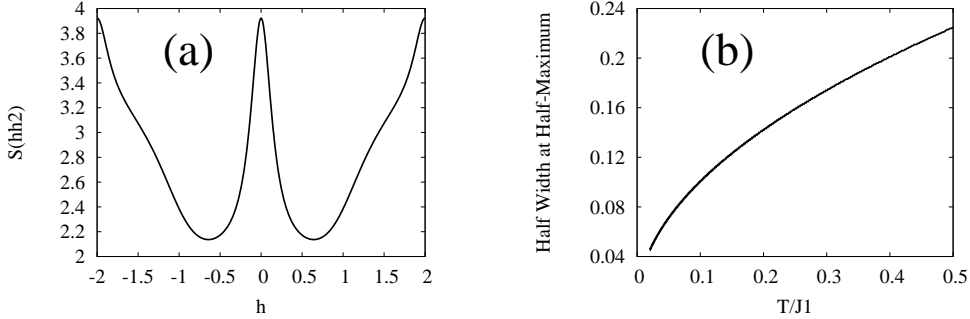


Figure 8: (a) The neutron scattering intensity along $(h h 2)$ for nearest neighbour spin ice at $T/J_1 = 0.5$. The half width at half-maximum is found by locating the minimum around $h = 0.5$ (I_{min}), then moving towards $h = 0$. When the function $I(h h 2) - \frac{(I(002) + I_{min})}{2}$ is minimized the value of h is recorded. (b) The half width at half-maximum of the pinch point as a function of temperature. A fit to the line $y = 0.32 x^{\frac{1}{2}}$ is indistinguishable by eye, with asymptotic standard error 0.01%.

This is the purpose of the next section.

3.1.3 Pinch-Point Temperature Dependence

In the nearest neighbour model, the pinch points at (002) and symmetry related locations broaden at finite temperature, and their width (half width at half-maximum, HWHM) is temperature dependent. It is often stated that the pinch points' widths are inversely related to real space correlation lengths [18, 26]. This makes intuitive sense, but no proof has yet appeared. Nevertheless, working with this idea we can consider the average distance between monopoles ξ to be given by $\xi^{-1} \sim \text{HWHM}$.

The width of the pinch points in the nearest neighbour model is straightforward to measure by taking a cut along $(h h 2)$, for example. The HWHM can then be found numerically for a range of temperatures. At low temperature I found the large N model to give a dependence $\xi^{-1} \propto T^{1/2}$, as is shown in Figure 8. This is in accordance with the results of [18, 26].

In the dipolar spin ice model the pinch points are infinitely sharp for all temperatures, and another method is required to find the dependence of ξ on T . Two suggestions were proposed by R. Moessner in private correspondence. The first method is to take a small contour about the pinch point, and to find the temperature dependence of the width of the resulting peak. The second method is to find the contrast between the intensity found by approaching the singularity along different directions. I treat these methods in turn.

Sticking to the plane $(h h l)$, I first considered the circular contour

$$l = 2 \pm \sqrt{w^2 - h^2} \quad (45)$$

where w is the radius of the circle traversed, and the path starts at $(\overline{ww}2)$. Taking the upper semicircle, with $w \lesssim 0.5$, the scattering intensity S as a function of the distance along the contour is approximately Lorentzian in form. The lower contour gives an almost indistinguishable plot. It was hoped that finding the HWHM of this Lorentzian as a function of temperature would yield some measure of $\xi(T)$, the pinch point ‘width’. Unfortunately, I found the HWHM to be completely independent of temperature across the range $\beta J_1 \in [0.01, 100]$. The magnitude of the intensity varies significantly across this range, but it does this so as to maintain the width of the Lorentzian peak.

To implement the second suggestion, I found the difference in intensity tending towards (002) along $(00l)$ and $(hh2)$. This gives a measure of the contrast at the pinch point; that is, how ‘singular’ the singularity is. I found a linear dependence on the contrast with temperature, over the same temperature range $\beta J_1 \in [0.01, 100]$. If this were really measuring the width of the pinch point the result would be quite unphysical, as we know from experiment that this temperature range encompasses the frozen ground state, the spin ice regime, and the high temperature paramagnetic regime. I suspect that the contrast is simply not a good measure of pinch point width. Furthermore, the linear temperature dependence of the contrast which I have found is almost certainly a relic of the model, rather than a physical result.

Neither of the above methods gave a good measure of the pinch point width’s temperature dependence. This is a problem with the large N model itself. At low temperature it would seem sensible for $\xi(T)$ to take an exponential form

$$\xi(T) \sim \exp(2 J_{eff}/T) \quad (46)$$

with $J_{eff} = J_1 + D_{nn}$ an effective coupling taking into account nearest neighbour and dipolar terms (see Section 2.3). I suggest this form as the low lying excitations consist of a single spin flip, requiring energy $2 J_{eff}$, and an Arrhenius law such as Equation 46 is often a good approximation to processes blocked by an activation energy barrier. This dependence is indeed reproduced by a ‘cluster variational method’ in reference [43]. Experiments attempting to distinguish the pinch points due to dipolar interactions from those due to the ice rules could do so by checking for this exponential temperature dependence on pinch point width.

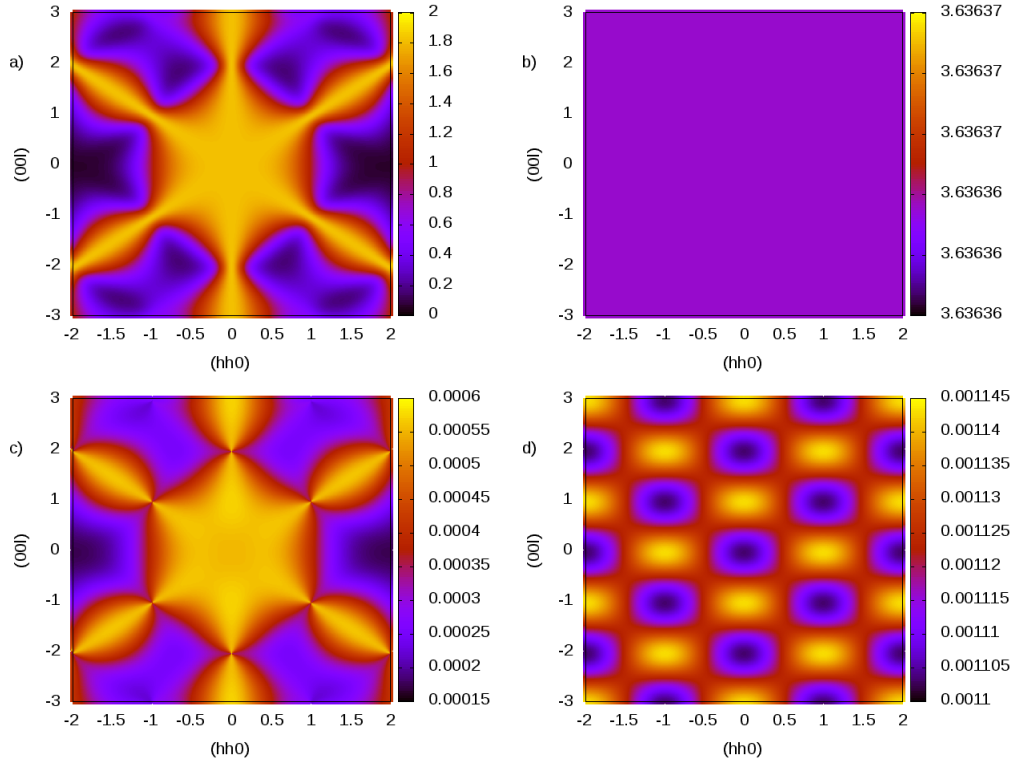


Figure 9: The spin flip (SF) and non-spin flip (NSF) neutron scattering patterns for: (a), (b) nearest neighbour spin ice; (c), (d) dipolar spin ice. The nearest neighbour case agrees with previous numerical results ([46] Figures 2 (a), (b)) whereas the dipolar case agrees with experimental results ([46] Figures 2 (d), (e)). All plots here are at temperature $T = 0.5 |J_1|$, and so can be compared directly with the unpolarized scattering patterns in my Figures 6 (d) and 7 (b). Note that the NSF nearest neighbour pattern is flat to 11 orders of magnitude.

3.1.4 Spin Flip and Non-Spin Flip Scattering

Neutrons are charge-neutral with a nonzero magnetic moment. Scattering factors referred to so far relate to the change in momentum of the neutrons as they traverse the crystal. By using a spin-polarized neutron beam it is possible to extract additional information about the crystal by measuring the rotation of the neutrons' spins. Spin-polarized measurements give information about magnetic correlations [44], which are of interest in this study.

Unpolarized neutron scattering results for spin ices suffer from suppressed scattering in the regions of the pinch points. A typical example is Figure 4 A of [45]. Fennell *et al.* in 2009 [46] (and, independently, Chang *et al.* [47, 48]) used polarized neutron beams to measure the scattering of spin flipped and non-spin flipped neutrons separately. They found that the pinch points are visible in the spin flipped pattern, but that they are obscured by corresponding regions of low intensity in the non-spin flipped pattern when unpolarized neutrons are used. They ran Monte Carlo simulations of the nearest

neighbour model and found that the spin flipped patterns agreed with experiment, but that the non-spin flipped numerical results showed no scattering. This, they argued, explained why theory was able to predict the pinch points before a well established experimental observation was made.

Based on Fennell's work [46, 49] I was able to calculate the spin flipped and non-spin flipped neutron scattering patterns for both the nearest neighbour model and the dipolar model. I chose $\hat{\mathbf{z}}$ along $[1\bar{1}0]$, perpendicular to the scattering plane (hhl) , and for a beam along $\mathbf{K} \in (hhl)$ I chose $\hat{\mathbf{x}} \parallel \mathbf{K}$ and $\hat{\mathbf{y}} \perp \mathbf{K}$. With these choices, the component $S_{yy}(\mathbf{K})$ gives the spin flipped scattering (SF) and $S_{zz}(\mathbf{K})$ the non-spin flipped scattering (NSF). From Equation 22, this gives the results:

$$\text{SF: } S_{yy}(\mathbf{K}) = \frac{1}{2l^2 + 4h^2} (l, l, -2h) \cdot M \cdot \Omega(\mathbf{K})^{-1} \cdot M^\dagger \cdot \begin{pmatrix} l \\ l \\ -2h \end{pmatrix} \quad (47)$$

$$\text{NSF: } S_{zz}(\mathbf{K}) = \frac{1}{2} (1, -1, 0) \cdot M \cdot \Omega(\mathbf{K})^{-1} \cdot M^\dagger \cdot \begin{pmatrix} 1 \\ -1 \\ 0 \end{pmatrix}. \quad (48)$$

With the nearest neighbour model I find agreement with the results of [46]. Figures 9 (a) and (b) show the SF and NSF scattering for this model, and can be compared with Figures 2 (d) and (e) of [46]. The NSF scattering is flat to eleven orders of magnitude. Using the dipole model, however, I found I was able to reproduce the experimental results to a good degree of accuracy. The experimental results are given in Figures 2 (a) and (b) of [46], and can be compared with my Figures 9 (c) and (d). This new result confirms the suggestion that it is dipolar interactions between spins which lead to the pinch point scattering observed to date, and not the ice rules.

3.2 The Heisenberg System $Y_2Mo_2O_7$

For the last part of my study I turn to the spin glass system yttrium molybdenate. Very recent (as yet unpublished) neutron scattering experiments conducted by C. Wiebe *et al.* at the University of Winnipeg have shown a ring of scattering in the (hhl) plane of radius $\simeq 0.44$. The ring persists to high temperatures, and is still very visible at 300 K. Some results are reproduced in Figure 10 with the kind permission of C. Wiebe. The new results are based on tests of a single crystal, and are consistent with previous work on powdered samples [50]. The methods developed in this report readily carry over to the $Y_2Mo_2O_7$ system, which consists of Heisenberg spins on a pyrochlore lattice. The dipolar interaction terms in this system are negligible, due to the relatively small magnetic moment of the Mo^{4+} ions ($1.5 - 2\mu_B$ [51]). Using the large N model for the

case of Heisenberg spins, we have the neutron scattering factor

$$S(\mathbf{k}) = (1, 1, 1, 1) \cdot \left[\left(\lambda \mathbf{1}_4 - \beta \sum_n J_n V^{(n)}(\mathbf{k}) \right)^{-1} \right] \cdot \begin{pmatrix} 1 \\ 1 \\ 1 \\ 1 \end{pmatrix} \quad (49)$$

with λ given by the self-consistency condition that the average length of each spin component must be one third:

$$\frac{1}{3} = \frac{1}{4N} \sum_{\mathbf{k} \in BZ} \text{Tr} \left[\lambda \mathbf{1}_4 - \beta \sum_n J_n V^{(n)}(\mathbf{k}) \right]^{-1}. \quad (50)$$

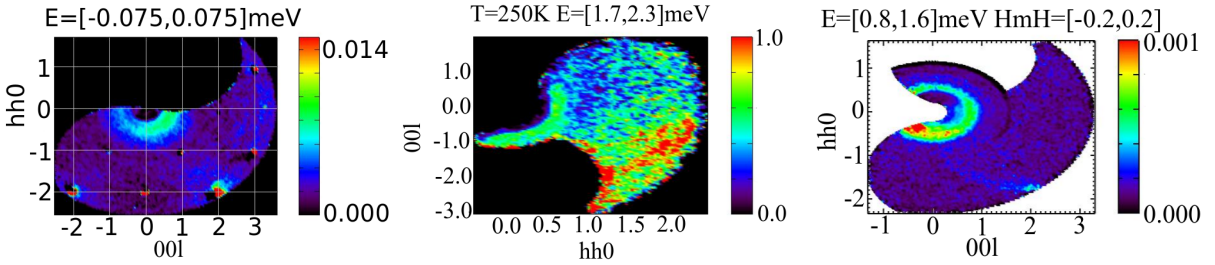


Figure 10: Experimental neutron scattering results reproduced with the kind permission of C. Wiebe. All images show a ring of scattering of radius $0.3 \lesssim |\mathbf{k}| < 1$. The central image is at $T = 250$ K, whereas the other images are at $T = 300$ K.

3.2.1 Next-Nearest Neighbour Terms

A ring of scattering of radius 0.44 in reciprocal space suggests real space correlations around the length of the conventional unit cell (Figure 4 (a)), but no further. I began by considering the case of first, second, and third nearest neighbour interactions, with $J_{n>4} = 0$. An important constraint on the couplings comes from the Curie-Weiss temperature of $Y_2Mo_2O_7$, which is $\Theta_{CW} \simeq -200$ K (the sign indicates antiferromagnetism). In general, to first order in J , we have the constraint [52, 53]:

$$\frac{S(S+1)}{3} (n_1 J_1 + n_2 J_2 + n_3 J_3) = \Theta_{CW} \quad (51)$$

where n_i is the number of i^{th} nearest neighbours, and $S(S+1)$ is $\langle S^2 \rangle$. In yttrium molybdenate there are 6 nearest neighbours and 12 each of 2^{nd} and 3^{rd} nearest neighbours. Hund's rules give $S = 1$ for Mo^{4+} , so the constraint becomes

$$4(J_1 + 2J_2 + 2J_3) = -200 \text{ K}. \quad (52)$$

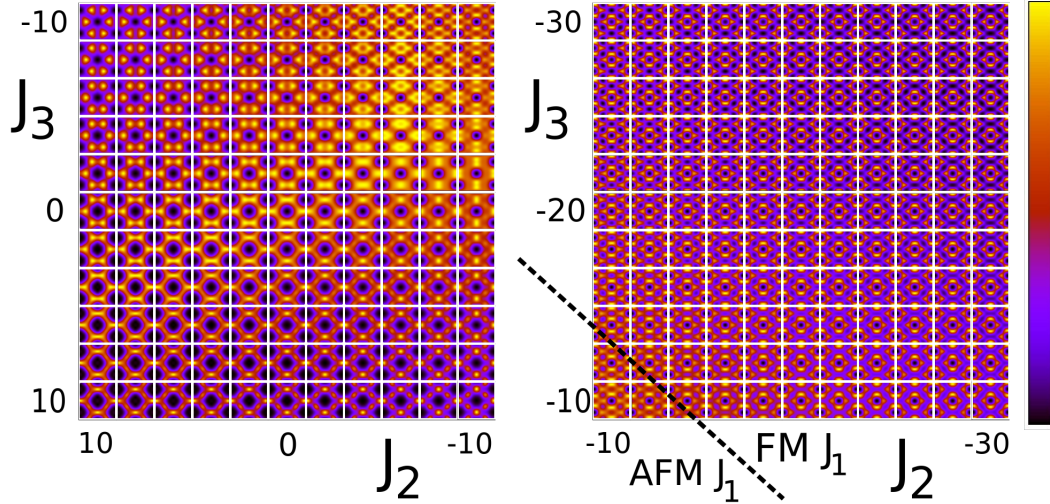


Figure 11: Neutron scattering plots in the (hhl) plane for $Y_2Mo_2O_7$ at $T = 150$ K, with a range of next nearest neighbour terms J_2, J_3 . Each plot covers $h \in [-2, 2]$, $l \in [-3, 3]$; the arbitrary scale of each plot is normalized to the colourbar on the right. The Curie Weiss constraint $4(J_1 + 2J_2 + 2J_3) = -200$ K is applied, meaning J_1 is ferromagnetic for $J_2 + J_3 < -25$. The approximate location of the transition is marked in the right hand diagram.

With this constraint applied I searched the parameter space $J_2, J_3 \in [-30 \text{ K}, 10 \text{ K}]$ ($\therefore J_1 \in [70 \text{ K}, -90 \text{ K}]$) in steps of 2 K for a similar ring of scattering in the (hhl) plane. I searched this range for temperatures $T = 10 \text{ K}, 50 \text{ K}, 100 \text{ K}, 150 \text{ K},$ and 200 K . A tabulation of the resulting scattering patterns at $T = 150 \text{ K}$ is shown in Figure 11, where it can be seen that no such ring was found. Some plots show a ring-like structure with a radius slightly greater than $|\mathbf{k}| = 1$, but as the ring never closes in towards the origin it would seem this is merely a coincidence. To eliminate the possibility that the ring exists in a narrow region of parameter space which was overlooked by this search it was necessary to find an analytic solution for the scattering. This is the purpose of the next section.

3.2.2 Analytic Solution

Having the form of the nearest neighbour interaction matrices (Appendix B) it is possible to obtain an analytic solution for the large N neutron scattering intensity. With an analytic solution the task of searching for a maximum in intensity reduces to the task of searching for a zero of the first derivative (with second derivative negative). Neutron scattering experiments show a circular ring of scattering in the (hhl) plane at a radius of around 0.44. As the ring is circular, there should be no loss of generality in searching the parameter space for a maximum intensity along the direction $(00l)$. For a fuller search of the parameter space I included 4^{th} nearest neighbour interactions. The total

interaction matrix now takes the following form:

$$\sum_{n=1}^4 J_n V^{(n)}(l) = \begin{pmatrix} D & A & A & B \\ A & D & B & A \\ A & B & D & B \\ B & A & B & D \end{pmatrix} \quad (53)$$

with

$$A = 2(J_1 + 2J_2 + J_4) \cos\left(\frac{\pi l}{2}\right) + 2J_4 \cos\left(\frac{3\pi l}{2}\right)$$

$$B = 2[J_1 + 2J_2 \cos(\pi l) + 2J_4]$$

$$D = 2[J_1 + 2J_2 + 4J_3(\cos(\pi l) - 1) + 2J_4].$$

The neutron scattering intensity is given by Equation 20. With a change of variables $A' = \beta A$, $B' = \beta B$, $D' = \lambda + \beta D$, this reduces to

$$S(l) = (1, 1, 1, 1) \cdot \begin{pmatrix} D' & A' & A' & B' \\ A' & D' & B' & A' \\ A' & B' & D' & B' \\ B' & A' & B' & D' \end{pmatrix}^{-1} \cdot \begin{pmatrix} 1 \\ 1 \\ 1 \\ 1 \end{pmatrix} \quad (54)$$

and with some algebra this gives the final expression:

$$S(l) = \frac{2(A' + B' - 2D')}{A'^2 + A'B' + B'^2 - (A' + B')D' - D'^2}. \quad (55)$$

The derivatives of Equation 55 do not take illuminating analytic forms. They can however be quickly evaluated numerically. To proceed, I wrote a FORTRAN code which searched for maxima of $S(l)$ (*i.e.* $\partial S/\partial l = 0$ and $\partial^2 S/\partial l^2 < 0$) in the domain $l \in [0.3, 0.6]$. The program searched a large region of parameter space: $J_2, J_3, J_4 \in [-30, 10]$, $T \in [1, 200]$, with the constraint $4(J_1 + 2J_2 + 2J_3 + 2J_4) = \theta_{CW} = -200K$ (including the twelve 4th nearest neighbours).

The search routine found some results matching the required conditions. Closer inspection revealed a small maximum around $l = 0.5$ which was overshadowed by a large peak at $l = 2$ in each case. I adjusted the requirement on the second derivative to give a more pronounced maximum, requiring $\partial^2 S/\partial l^2 < -0.04$, and further stipulated that there must be no other maxima at higher l . Applying these conditions returned no results in the stated parameter range, suggesting the nearest neighbour model is insufficient to explain the experimental data.

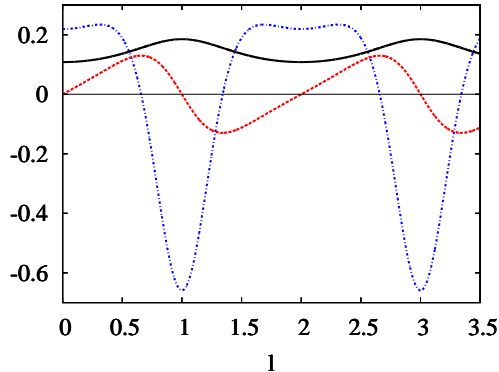


Figure 12: Plots along $(00l)$ of the neutron scattering intensity S (black, solid), the first derivative $\partial S/\partial l$ (red, dashed), and the second derivative $\partial^2 S/\partial l^2$ (blue, dot-dashed). All plots are for $T/J_1 = 50$, with $J_2/J_1 = 30$ and $J_3/J_1 = 25$. The Lagrange multiplier was set artificially high at $\lambda = 50$ (see Section 3.2.2 for discussion).

One possible loophole in the program, which I mention for completeness, was in the evaluation of the Lagrange multiplier λ . Due to time and processing constraints it was not possible for me to accurately determine λ for each loop of the program. Instead I set the value to a high enough level that it was guaranteed to be larger than the correct value. The effect of a large λ is to ‘smear out’ the scattering pattern in a similar manner to an increased temperature. Indeed, in the case $J_{n>1} = 0$, changing λ literally acts to renormalize the temperature in this manner. With further neighbour interactions this is not quite true, but after many numerical checks it seems that too high a λ will not change the qualitative behaviour of $S(l)$; specifically, the zeroes of $\partial S/\partial l$ are unaffected. Sample plots of the analytic solution and its first two derivatives are provided in Figure 12 for comparison with previous numerical plots.

4 Conclusions and Further Work

Research on spin ices is a very new field, dating back less than a decade. The existence of a Coulomb phase in spin ices is widely accepted, but still lacks a full theoretical and experimental backing. The previously accepted idea was that ‘pinch points’ in neutron scattering data are a demonstration of the enforcement of the ice rules (a 2-in 2-out spin configuration on each pyrochlore tetrahedron). If this were true it would make a good case for the existence of the Coulomb phase, as violations of the ice rules at finite temperature take the form of monopole anti-monopole pairs. However, pinch points are now known to exist into the high temperature paramagnetic regime, meaning they can be produced by dipolar interactions in the absence of the ice rules. In this report I

considered alternative evidence, using both the nearest neighbour and dipolar models of spin ice in an attempt to expose peculiarities of the theory which could demonstrate the existence of the Coulomb phase.

I first attempted to find some measure of pinch point width which could be used to isolate the contributions from dipolar interactions and ice rule enforcement. Pinch points in the dipolar model are infinitely sharp at all temperatures, so I tried some alternative measures of width in order to find a temperature dependence. While the methods may be sound, the results were inconclusive as a result of the large N model's inability to give a quantitatively accurate temperature dependence.

By considering the case of spin flipped (SF) and non-spin flipped (NSF) neutron scattering, I provided further evidence in support of the idea that dipolar interactions between spins must be taken into account to reproduce experimental results. I demonstrated that the large N method applied to the nearest neighbour spin ice model leads to a flat NSF scattering pattern, whereas applying large N to the dipolar model reproduces the checkerboard pattern seen in experiment.

One possible future route for exposing the Coulomb phase in spin ice is to focus on the network of Dirac strings. Monopoles are freely diffusing in nearest neighbour spin ice, or have a Coulomb's law interaction in dipolar spin ice. In the $U(1)$ gauge model the string network is believed to renormalize the diffusion coefficient for monopoles [17, 54]. Evidence for monopoles and the string network could be found by substantiating this claim. A possible method could involve tempering the material by application of a magnetic field. If we were to cool the crystal from high temperature we would expect a state consisting of monopoles in a disordered and tangled network of strings, leading to a small diffusion coefficient. Applying a sufficiently high magnetic field along a symmetry direction such as [100] can lead to 2-in 2-out ice rule enforcement across the whole material [10, 55, 56], removing information about the string network. Removing the field again should end in the same population of monopoles as before, but with a less tangled string network, and a higher diffusion coefficient. The diffusion coefficient can be inferred from a. c. susceptibility measurements [39, 57] and neutron scattering data [17, 58].

Recent work [59] suggests that thermal quenches from the high temperature paramagnetic regime to deep into the spin ice regime can lead to 'non-contractible' defect pairs. These are monopole anti-monopole pairs in neighbouring tetrahedra which cannot annihilate due to the string network. Flipping the spin connecting these tetrahedra would change them from 3-in 1-out (and vice versa) to 4-in 0-out (0-out 4-in), rather than the desired 2-in 2-out. It is not known whether the cooling rates required are unfeasible or unavoidable [39]. If the latter case is true, this gives some hope that the tempering method could give some demonstration of the Coulomb phase.

The spin glass material $Y_2Mo_2O_7$ has recently been found to exhibit a ring of scattering of radius $\simeq 0.44$ in the (hhl) plane. Research into this phenomenon has not formerly begun. I attempted to reproduce this result by applying the large N method to the nearest neighbour model of spin glass. As dipolar effects are negligible in $Y_2Mo_2O_7$ the nearest neighbour model is expected to be quite accurate for this material. Using the exact solution for the neutron scattering I was able to show that the ring of scattering cannot be reproduced by this model, meaning something of the physical system is being neglected in this treatment.

To extend the nearest neighbour model there are two alterations which should first be considered. The first is to allow the two inequivalent types of 3^{rd} nearest neighbour to have different coupling strengths J_{3a} and J_{3b} . The possibility is considered in reference [24], but not with specific reference to this problem. The second extension is to include 5^{th} nearest neighbours. Although the contribution from these neighbours should be small, there are 24 of them. They are the furthest neighbours which fit in the conventional unit cell, and are therefore around the distance required to generate the observed peak in reciprocal space.

If it turns out that additional processes must be considered, there are again two options which should be considered before all others. The first is to take into account the *Onsager reaction field* [60, 61]. The large N and mean field treatments considered in this report assume that the spin at site i feels a mean field from all the other spins in the lattice, which contribute equally. In reality, the neighbouring spins are likely to be ‘pulled along’ with \mathbf{s}_i , acting to screen the remaining field. Including the Onsager reaction field in the scattering calculation may give a possible method of localizing the ring to the observed radius. The second correction to the model considered is to include quantum mechanical effects, which were completely neglected throughout this paper. A possible quantum correction of interest takes the form of an additional term in the Hamiltonian favouring nematicity of spins:

$$\mathcal{H} = \mathcal{H}_0 - K \sum_{\langle ij \rangle} (\mathbf{s}_i \cdot \mathbf{s}_j)^2$$

with K a small positive term, encouraging alignment.

5 Acknowledgments

I would like to thank my supervisor M. J. P. Gingras for his supervision and regular advice. I would also like to thank T. Lin and J. Thompson for many useful discussions and for running Monte Carlo simulations in order to check my results, and R. Hill for explaining and demonstrating various experimental techniques. I would like to thank

S. Popescu for explaining the subtleties of the thermodynamics of the ferromagnet. I acknowledge the helpful advice of many of the other members of the PSI 2011 group and, in particular, B. Amorim, S. Montes Valencia, and D. Genkina. Finally, I would like to thank C. Wiebe for use of his group’s unpublished experimental data.

A Lattice Definitions

I will list here lattice conventions used in this report. In all cases, Roman letters run from 1-3, and Greek letters run from 1-4. Lengths of real space vectors are in units of the conventional unit cell length (Figure 4 (a)). The choice of unit cell outlined here contains four tetrahedra and sixteen spins. The three FCC basis vectors are denoted by \mathbf{R}^a , with \mathbf{R}^α also including the origin. The three sublattice vectors are denoted by \mathbf{r}^a , with \mathbf{r}^α including the origin. The four local Ising $\langle 111 \rangle$ axes are denoted by \mathbf{z}^α . It will sometimes be necessary to refer to these four vectors as a 4×3 matrix, $M^{a\alpha} = [\mathbf{z}^\alpha]^a$. The reciprocal lattice vectors for this choice of basis are denoted by \mathbf{G}^a . These conventions are summarized in Table 1.

FCC basis vect. \mathbf{R}^a	sublatt. vect. \mathbf{r}^a	local Ising dir. \mathbf{z}^α	recip. latt. vect. \mathbf{G}^a
$\mathbf{R}^1 = \frac{1}{2}[011]$	$\mathbf{r}^1 = \frac{1}{4}[011]$	$\mathbf{z}^1 = \frac{1}{\sqrt{3}}[111]$	$\mathbf{G}^1 = (\bar{1}11)$
$\mathbf{R}^2 = \frac{1}{2}[101]$	$\mathbf{r}^2 = \frac{1}{4}[101]$	$\mathbf{z}^2 = \frac{1}{\sqrt{3}}[1\bar{1}\bar{1}]$	$\mathbf{G}^2 = (1\bar{1}\bar{1})$
$\mathbf{R}^3 = \frac{1}{2}[110]$	$\mathbf{r}^3 = \frac{1}{4}[110]$	$\mathbf{z}^3 = \frac{1}{\sqrt{3}}[\bar{1}\bar{1}\bar{1}]$	$\mathbf{G}^3 = (11\bar{1})$
$\mathbf{R}^\alpha = \{\mathbf{R}^a, [000]\}$	$\mathbf{r}^\alpha = \{\mathbf{r}^a, [000]\}$	$\mathbf{z}^4 = \frac{1}{\sqrt{3}}[\bar{1}\bar{1}1]$	$\mathbf{G}^\alpha = \{\mathbf{G}^a, (000)\}$

Table 1: Lattice conventions used in this report.

B Interaction Matrices

The adjacency matrices $A^{(n)}(\mathbf{k})$ are given by the Fourier transform of the structure formed by n^{th} nearest neighbours on the pyrochlore lattice [26, 62]. I provide the first four here, using the convention of P. H. Conlon of adding multiples of the identity in order to interpret the Lagrange multiplier of Section 2.2 as a stiffness. The resulting matrices are termed ‘interaction matrices’ $V^{(n)}(\mathbf{k})$ by Conlon, and I have kept that convention. The stiffness condition requires $M \cdot V^{(n)}(\mathbf{0})$ to be a matrix of zeroes. I have converted k -space vectors to Miller indices by dividing by 2π , *i.e.* $(h, k, l) = (k_x, k_y, k_z)/2\pi$. All matrices listed are real and symmetric. There are two inequivalent sets of third nearest neighbours which could in theory have different couplings. Throughout this paper I have taken the two couplings to be equal. For a discussion of the effects of varying these couplings, see reference [24].

Defining the convention $\cos\left(\frac{\pi}{2}(x+y+z)\right) = C_{x,y,z}$, with $\bar{x} = -x$:

$$A^{(1)}(h, k, l) = 2 \begin{pmatrix} 0 & C_{k,l} & C_{h,l} & C_{h,k} \\ C_{l,k} & 0 & C_{\bar{h},\bar{k}} & C_{\bar{h},\bar{l}} \\ C_{h,l} & C_{\bar{h},\bar{k}} & 0 & C_{\bar{k},\bar{l}} \\ C_{h,k} & C_{\bar{h},\bar{l}} & C_{\bar{k},\bar{l}} & 0 \end{pmatrix}$$

$$A^{(2)}(h, k, l) = 2 \begin{pmatrix} 0 & (C_{2h,\bar{k},l} + C_{k,2h,\bar{l}}) & (C_{\bar{h},2k,l} + C_{h,2k,\bar{l}}) & (C_{\bar{k},2l,h} + C_{k,2l,\bar{h}}) \\ (C_{2h,\bar{k},l} + C_{k,2h,\bar{l}}) & 0 & (C_{h,k,2l} + C_{h,k,\bar{2}l}) & (C_{h,2k,l} + C_{h,\bar{2}k,l}) \\ (C_{\bar{h},2k,l} + C_{h,2k,\bar{l}}) & (C_{h,k,2l} + C_{h,k,\bar{2}l}) & 0 & (C_{2h,k,l} + C_{\bar{2}h,k,l}) \\ (C_{\bar{k},2l,h} + C_{k,2l,\bar{h}}) & (C_{h,2k,l} + C_{h,\bar{2}k,l}) & (C_{2h,k,l} + C_{\bar{2}h,k,l}) & 0 \end{pmatrix}$$

$$A^{(3)}(h, k, l) = 2 \text{diag} (C_{2h,2k} + C_{2h,2l} + C_{2k,2l} + C_{2h,\bar{2}k} + C_{2h,\bar{2}l} + C_{2k,\bar{2}l})$$

$$A^{(4)}(h, k, l) = 2 \begin{pmatrix} 0 & (C_{3k,\bar{l}} + C_{3l,\bar{k}}) & (C_{3h,\bar{l}} + C_{3l,\bar{h}}) & (C_{3h,\bar{k}} + C_{3k,\bar{h}}) \\ (C_{3k,\bar{l}} + C_{3l,\bar{k}}) & 0 & (C_{3h,k} + C_{3k,h}) & (C_{3h,l} + C_{3l,h}) \\ (C_{3h,\bar{l}} + C_{3l,\bar{h}}) & (C_{3h,k} + C_{3k,h}) & 0 & (C_{3k,l} + C_{3l,k}) \\ (C_{3h,\bar{k}} + C_{3k,\bar{h}}) & (C_{3h,l} + C_{3l,h}) & (C_{3k,l} + C_{3l,k}) & 0 \end{pmatrix}$$

$$\begin{aligned} V^{(1)}(\mathbf{k}) &= A^{(1)}(\mathbf{k}) + 2\mathbf{1}_4 \\ V^{(2)}(\mathbf{k}) &= A^{(2)}(\mathbf{k}) + 4\mathbf{1}_4 \\ V^{(3)}(\mathbf{k}) &= A^{(3)}(\mathbf{k}) - 12\mathbf{1}_4 \\ V^{(4)}(\mathbf{k}) &= A^{(4)}(\mathbf{k}) + 4\mathbf{1}_4. \end{aligned}$$

The distribution of n^{th} nearest neighbours is given in Table 2.

Neighbour	Distance	Number	Coupling
1 st	$\frac{\sqrt{2}}{4} a$	6	J_1
2 nd	$\sqrt{\frac{3}{8}} a$	12	J_2
3 rd	$\frac{\sqrt{2}}{2} a$	6 + 6	$J_3 = J_{3a} = J_{3b}$
4 th	$\frac{\sqrt{10}}{4} a$	12	J_4

Table 2: The distribution of n^{th} nearest neighbours in the pyrochlore lattice. Distances are in terms of the conventional unit cell length a . The two inequivalent 3rd nearest neighbours are taken to have the same coupling in this report.

References

- [1] P. A. M. Dirac, PROC. ROY. SOC. **A 133**, 60 (1931)
- [2] S. Eidelman *et al.* (Particle Data Group), PHYS. LETT. **B 592**, 1 (2004)
- [3] O. Tchernyshyov, NATURE **451**, 22-23 (2008)
- [4] C. Castelnovo, R. Moessner, and S. L. Sondhi, Nature **451**, 42-45 (2008)
- [5] L. D. C. Jaubert, M. Haque, and R. Moessner, ARXIV:1103.5397v1 (2011)
- [6] C. L. Henley, ANNU. REV. CONDENS. MATTER PHYS. **1**, 179–210 (2010)
- [7] M. E. Peskin and D. V. Schroeder, AN INTRODUCTION TO QUANTUM FIELD THEORY, Westview Press (1995)
- [8] L. Balents, NATURE **464**, 199-208 (2010)
- [9] M. J. Lawler, ARXIV:1104.0721 (2011)
- [10] D. J. P. Morris *et al.*, SCIENCE **326**, 411-414 (2009)
- [11] L. Pauling, J. AM. CHEM. SOC. **57 (12)**, 2680–2684 (1935)
- [12] J. D. Bernal and R. H. Fowler, J. CHEM. PHYS. **1**, 515 (1933)
- [13] V. M. Nield and R. W. Whitworth, J. PHYS.: CONDENS. MATTER **7**, 8259-8271 (1995)
- [14] J. Villain, SOLID STATE COMMUN., **10**, 967-970 (1972)
- [15] C. L. Henley, PHYS. REV. LETT. **96**, 047201 (2006)
- [16] N. W. Ashcroft and N. D. Mermin, SOLID STATE PHYSICS, Harcourt (1976)
- [17] L. D. C. Jaubert and P. C. W. Holdsworth, J. PHYS.: CONDENS. MATTER **23**, 164222 (2011)
- [18] C. L. Henley, PHYS. REV. **B 71**, 014424 (2005)
- [19] M. Elhajal, B. Canals, and C. Lacroix, PHYS. REV. **B 66**, 014422 (2002)
- [20] J. E. Greedan *et al.*, PHYS. REV. **B 79**, 014427 (2009)
- [21] R. W. Youngblood and J. D. Axe, Phys. Rev. B **23**, 232-238 (1981)
- [22] S. V. Isakov, R. Moessner, and S. L. Sondhi, PHYS. REV. LETT. **95**, 217201 (2005)

- [23] H. E. Stanley, *PHYS. REV.* **176** (2), 718-722 (1968)
- [24] P. H. Conlon and J. T. Chalker, *PHYS. REV.* **B 81**, 224413 (2010)
- [25] P. H. Conlon, Ph.D. Thesis, Oxford University (2010)
- [26] S. Isakov, Ph.D. Thesis, Stockholm University (2004)
- [27] P. P. Ewald, *ANN. PHYS.* **369**, 253–287 (1921)
- [28] M. Enjalran and M. J. P. Gingras, *PHYS. REV.* **B 70**, 174426 (2004)
- [29] M. Enjalran and M. J. P. Gingras, *ARXIV:COND-MAT/0307151v1* (2003)
- [30] M. J. P. Gingras and B. C. den Hertog, *CAN. J. PHYS.* **79**, 1339–1351 (2001)
- [31] A. G. Del Maestro, Master’s Thesis, University of Waterloo (2003)
- [32] L. D. C. Jaubert, Ph.D. Thesis, École Normale Supérieure de Lyon (2009)
- [33] R. G. Melko, B. C. den Hertog, and M. J. P. Gingras, *PHYS. REV. LETT.* **87**, 067203 (2001)
- [34] B. C. den Hertog and M. J. P. Gingras, *PHYS. REV. LETT.* **84**, 3430-3433 (2000)
- [35] S. T. Bramwell, *J. PHYS.: CONDENS. MATTER* **23**, 112201 (2011)
- [36] S. T. Bramwell *et al.*, *NATURE* **461**, 956-960 (2009)
- [37] S. Sondhi, *NATURE* **461**, 888-889 (2009)
- [38] S. R. Giblin *et al.*, *NATURE PHYS.* **7**, 252-258 (2011)
- [39] J. A. Quilliam *et al.*, *PHYS. REV.* **B 83**, 094424 (2011)
- [40] L. D. C. Jaubert and P. C. W. Holdsworth, *NATURE PHYS.* **5**, 258-261 (2009)
- [41] R. Moessner and S. L. Sondhi, *PHYS. REV.* **B 68**, 064411 (2003)
- [42] J. P. Clancy *et al.*, *PHYS. REV.* **B 79**, 014408 (2009)
- [43] S. Yoshida, K. Nemoto, and K. Wada, *J. PHYS. SOC. JPN.* **71**, 948-954 (2002)
- [44] A. Furrer, J. Mesot, and T. Strässle, *NEUTRON SCATTERING IN CONDENSED MATTER PHYSICS*, World Scientific (2009)
- [45] S. T. Bramwell and M. J. P. Gingras, *SCIENCE* **294**, 1495-1501 (2001)

- [46] T. Fennell *et al.*, Science **326**, 415-417 (2009)
- [47] L. J. Chang *et al.*, J. PHYS.: CONF. SER. **211**, 012013 (2010)
- [48] L. J. Chang *et al.*, PHYS. REV. **B 82**, 172403 (2010)
- [49] T. Fennell *et al.*, Supplementary Online Material for [46]
- [50] J. S. Gardner *et al.*, Nuclear Engineering and Technology **43**, 7-13 (2011)
- [51] N. P. Raju, E. Gmelin, and R. K. Kremer, PHYS. REV. **B 46**, 5405–5411 (1992)
- [52] A. L. Cornelius and J. S. Gardner, PHYS. REV. **B 64**, 060406 (2001)
- [53] C. Kittel, INTRODUCTION TO SOLID STATE PHYSICS, 8th Ed., Wiley (2005)
- [54] C. Phatak *et al.*, PHYS. REV. **B 83**, 174431 (2011)
- [55] D. Slobinsky *et al.*, PHYS. REV. LETT. **105**, 267205 (2010)
- [56] M. J. P. Gingras, SCIENCE **326**, 375-376 (2009)
- [57] J. Snyder *et al.*, PHYS. REV. **B 69**, 064414 (2004)
- [58] T. Fennell *et al.*, PHYS. REV. **B 72**, 224411 (2005)
- [59] C. Castelnovo, R. Moessner, and S. L. Sondhi, PHYS. REV. LETT. **104**, 107201 (2010)
- [60] R. M. White, QUANTUM THEORY OF MAGNETISM: MAGNETIC PROPERTIES OF MATERIALS, 3rd Ed., Springer (2007)
- [61] D. Hohlwein and J. Hoffmann, Phys. Rev. **B 68**, 140408 (2003)
- [62] J. N. Reimers, A. J. Berlinsky, and A. -C. Shi, PHYS. REV. **B 43**, 865-878 (1991)